

Will be published in "Astronomy Letters", 2011, v.37, N4, pp. 233-247

Modeling the Images of Relativistic Jets Lensed by Galaxies with Different Mass Surface Density Distributions

T.I.Larchenkova^{1,*}, A.A.Lutovinov^{2,}, and N.S.Lyskova³**

*Astro Space Center, Lebedev Physical Institute, Russian Academy of Sciences,
Profsoyuznaya str., 84/32, Moscow, 117997 Russia¹*

*Space Research Institute, Russian Academy of Sciences, Profsoyuznaya str., 84/32,
Moscow, 117997 Russia²*

*Moscow Institute of Physics and Technology, Institutskii per. 9, Dolgoprudnyi, Moscow
obl., 141700 Russia³*

Received on 22 June 2010

The images of relativistic jets from extragalactic sources produced by gravitational lensing by galaxies with different mass surface density distributions are modeled. In particular, the following models of the gravitational lens mass distribution are considered: a singular isothermal ellipsoid, an isothermal ellipsoid with a core, two- and three-component models with a galactic disk, halo, and bulge. The modeled images are compared both between themselves and with available observations. Different sets of parameters are shown to exist for the gravitationally lensed system B0218+357 in multicomponent models. These sets allow the observed geometry of the system and the intensity ratio of the compact core images to be obtained, but they lead to a significant variety in the Hubble constant determined from the modeling results.

Key words: relativistic jets, gravitational lensing, B0218+357

* e-mail: tanya@lukash.asc.rssi.ru

** e-mail: aal@hea.iki.rssi.ru

INTRODUCTION

The formation and physical properties of largescale relativistic plasma jets from active galactic nuclei, quasars, and radio galaxies are among the topical questions of modern extragalactic astronomy. The relativistic jet from the giant elliptical galaxy M87 whose distance is 16.7 Mpc has been studied most extensively owing to its close spatial location. The question of whether the observed one-sided jet is the result of its motion directed toward the observer, whereby the jet knots move with a speed close to the speed of light and their emission is more intense than that of the counterjet due to the Doppler effect, or the emission is actually anisotropic remains without an answer so far.

Using the gravitational lensing of distant galactic nuclei, quasars, and compact regions of radio galaxies with large-scale relativistic jets not only gives the observers a unique opportunity to see such astrophysical objects but also will, possibly, allow individual features of their jets, for example, the counterjet unobservable in the absence of lensing, to be studied in future. It is well known that the gravitational lensing of a compact source with a relativistic jet can give rise to multiple images of the source itself and its extended jet. Such gravitationally lensed systems are actually observed at present. MG 1131+0456 (Hewitt et al. 1988), PKS 1830-211 (Nair et al. 1993), and B0218+357 (Patnaik et al. 1993, 1995) are the brightest of them in the radio band. Therefore, modeling the images of these sources and investigating their behavior with time becomes a topical task. The planned launches of very long baseline space interferometers with a high angular resolution make this task important and timely. Comparison of the simulations of gravitationally lensed sources with observational data will provide additional information both about the physical radiation processes and collimation mechanisms and about the mass density distribution in the lens object.

The source B0218+357 is of particular interest among the listed gravitationally lensed systems with relativistic jets. The presence of a largescale jet with an extent of ~ 1 Mpc observed in the radio band, its considerable distance from other extragalactic sources, and the accurately measured time delay between its images (Biggs et al. 1999; Cohen et al. 2000) make the study of this object attractive, among other things, for an independent determination of the Hubble constant: first, the source lies at a high redshift at which the peculiar velocities are lower than the velocities of the Hubble law; second, measuring the Hubble constant from the time delay is a direct method of measurement, i.e., the geometric scale of the gravitationally lensed system is measured directly (Narayan and Bartelmann 1996). Note that the lens in this system is a spiral galaxy (Browne et al. 1993). This is a rare event per se, because most of the gravitational lenses known to date are elliptical galaxies. Apart from B0218+357, only nine systems in which the lens is a spiral galaxy are known to date (Feron et al. 2009).

The shape distortion and the appearance of multiple images of a relativistic jet in the case of its gravitational lensing by a galaxy are of interest in the study. In particular, how important is it to take into account the multicomponent structure of the spiral galaxy when it lenses the jet? How will the noncoaxiality of the galactic components affect the picture of lensing? Under which conditions for gravitational lensing of the jet do ring structures

emerge in the image? Is the assumption that the observed “radio rings” are the images of the lensed jet justified? Investigating these questions is the goal of our paper.

It seems natural to investigate the gravitational lensing of a jet separately by early- and late-type galaxies. Therefore, we will consider models of the mass surface density distribution in elliptical and spiral lens galaxies. In the case of elliptical galaxies, either a homeoidal elliptical mass surface density distribution or an elliptical effective lensing potential are considered (see, e.g., Kassiola and Kovner 1993; Kormann et al. 1994). For a homeoidal density distribution, all surfaces of equal density are represented by concentric, similar, and identically oriented ellipsoids (King 2002). In this paper, when modeling both elliptical and spiral galaxies, we use models of the mass surface density distribution rather than the effective potential, because the models with an elliptical potential are inapplicable at high ellipticities (Kormann et al. 1994).

For spiral lens galaxies, Keeton and Kochanek (1998) suggested using models including their multicomponent structure, namely, their disk, bulge, and halo. In this paper, when modeling the gravitational lensing of a relativistic jet by a spiral galaxy, we will use the models proposed in the paper mentioned above. The choice of the models is dictated by the fulfilment of the following main requirements: an adequate physical description of the observed phenomena and the possibility of representing the lens equation in analytic form (the existence of a twice continuously differentiable lensing potential).

The gravitational lensing of an infinitely thin relativistic jet for elliptical lens galaxies described by the models of a singular isothermal ellipsoid and an ellipsoid with a core are considered in Section 1. The gravitational lensing of a jet by a spiral galaxy is investigated in Section 2. In particular, we consider the model of a disk and a softened halo located in an isothermal dark matter halo for various values of their parameters; the Kuzmin model of a disk (Kuzmin 1956) in an isothermal halo; and the model of a disk and bulge in an isothermal halo. Apart from investigating the images of a relativistic jet that appear when it is gravitationally lensed by galaxies described by both one-component and two-components models of the mass surface density distribution, the images emerging in various models are also compared qualitatively in the first two sections of the paper. For an adequate comparison, it is necessary to fix the spatial location of the relativistic jet whose choice is relatively arbitrary but the same for all models. In the succeeding sections, when investigating the possibility of the formation of ring structures as a result of the jet lensing, we remove the requirement for its fixed spatial location. The emerging images of the relativistic counterjet for the models considered in Sections 1 and 2 are modeled in Section 3. The application of our results to the source B0218+357 is discussed in Section 4. In Conclusions, we summarize our results and discuss their possible applications.

GRAVITATIONAL LENS MODELS

A detailed description of the theory of gravitational lenses can be found in the book by Schneider et al. (1999). Here, we provide only the basic definitions needed for the subsequent understanding.

The lens equation maps the points of the lens plane to the corresponding points of the source plane. For all of the models considered here, the lens equation will be written in dimensionless variables normalized to the Einstein-Chwolson radius. The expression for it is written out in the Appendix (Eq. A1).

The ratio of the flux density received by the observer to the flux density that the observer would receive in the absence of a lens is called the lens magnification. The curve in the lens plane at each point of which the lens magnification becomes infinite is called a critical one. The curve in the source plane that is the mapping of the critical curve is called a caustic.

For the observed radio sources with compact images and an extended ringlike structure, one of the possible interpretations of their appearance is the situation where they are lensed by a galaxy. In this case, the compact images correspond to the image of the source’s central core and the extended structure is associated with the image of the relativistic jet. Generally, galaxies of various types can act as lenses, but here we consider models for elliptical and spiral galaxies. The expressions for the lensing potential and image magnification and the lens equation are given in the Appendix, because they are cumbersome. The lens equations for all models written out in analytic form were solved numerically by the so-called grid method where the region of presumed solutions was scanned with a sufficiently small step. The grid step was chosen to be 10^{-4} in both coordinates; the residual of the solution obtained is better than 10^{-7} .

The relativistic jet is represented as an infinitely thin segment with a constant radiation intensity at each of its points. The jet inclination α is measured from the x axis counter-clockwise. The choice of the jet inclination and the initial point of the jet are arbitrary, but the tangential caustic crossing condition is met in all of the models considered here. As our analysis shows (see below), displacing the initial point from the symmetry axis does not change fundamentally the shape of the images; only the positions of the initial points of the images and their number change (when the initial point of the jet is located outside the tangential caustic).

When modeling the jet images, we used the geometrical optics approximation, which, as any approximation, has its limitations. First, the light beams coming from the lensed object to the observer may turn out to be coherent, which will lead to interference between these beams. Second, the magnification of a point source as the latter approaches the caustic tends to infinity. Despite these shortcomings, in an overwhelming majority of the cases of gravitational lensing, the geometrical optics approximation is justified and the corrections introduced by wave optics are significant only for very compact sources, for example, extragalactic pulsars. This question was studied in detail in the book by Schneider et al. (1999). Here, we will only give an upper limit on the magnification that emerges when the jet approaches the tangential caustic from wave optics. In the model of an infinitely thin axisymmetric lens and the approximation of a point source located near the astroid at a cosmological distance, we can estimate the maximum magnification defined by the expression (Schneider et al. 1999)

$$\mu_{max} \sim \left(\frac{M}{M_{\odot}}\right)^{1/3} \left(\frac{\lambda}{10^6}\right)^{-1/3}, \quad (1)$$

where M is the lens mass and λ is the wavelength expressed in centimeters. For lenses with a mass $M \sim 10^{10} M_\odot$ in the radio band ($\lambda \sim 1$ cm), we obtain

$$\mu_{max} \sim 10^{5-6}.$$

As we see, the magnification is not infinite but very high, which introduces no changes in the results obtained here.

1. MODELS FOR ELLIPTICAL GRAVITATIONAL LENS GALAXIES

As was noted in the Introduction, in most of the observed gravitational lensing events with the appearance of multiple images, the lenses are elliptical galaxies that are described by the models of either an elliptical density or an elliptical effective lensing potential. An elliptical lens galaxy is best described by the models of an isothermal singular ellipsoid and an isothermal ellipsoid with a core. The shape of the critical and caustic curves for these models was studied in detail by Kormann et al. (1994).

Since the general expressions for the ellipsoid potential are reduced only to elliptic integrals, we will consider the special case of an ellipsoid - a spheroid for which the expressions can be written via elementary functions (Schmidt 1956). Let us introduce the main notation and parameters used in the models under consideration. Let q_3 be the axis ratio of the spheroid. Its projection onto the plane perpendicular to the line of sight to the source is then an ellipse with the axis ratio $q = \sqrt{q_3^2 \cos^2(i) + \sin^2(i)}$, where i is the inclination of the spheroid. The angle $i = 0^\circ$ implies that we see the spheroid edge-on; if, alternatively, $i = 90^\circ$, then the projection of the spheroid onto the plane is a circle.

The lens equation, the expressions for the lensing potential, i.e., for the projection of the three dimensional potential onto the lens plane, and the image magnification are given in the Appendix (Eqs. A2 and A3).

The modeling results for a singular isothermal ellipsoid and an ellipsoid with a core are presented in Fig. 1. To be able to conveniently compare the cases considered in the figure, we chose equal inclinations of the jet α and its length of 60° and ~ 1.5 Einstein-Chwolson radius, respectively. The dark gray and light-gray lines indicate the caustic and critical curves, respectively; the black line indicates the relativistic jet projected onto the lens plane. The color of the jet images correspond to different magnifications. Purple color is used to denote regions where the absolute value of the magnification is less than 1, blue is for magnifications changing from 1 to 3, green - from 3 to 7, yellow - from 7 to 10, and red is for magnifications greater than 10. The upper and lower case letters denote some of the reference points on the jet and the corresponding points on the images, respectively.

The radiation intensity along the jet is assumed to be constant in all of the models under consideration, which, of course, disagrees with available observations. However, if the magnification at each point of the jet is known, then the intensity distribution can be derived from its images by specifying an arbitrary intensity distribution along the jet.

Consider the model of an isothermal ellipsoid with a core $s = 0.3$ and spheroid axis ratios typical of elliptical galaxies, $q_3 = 0.3$ (Fig. 1a) and $q_3 = 0.6$ (Fig. 1b). We see that as the parameter q_3 increases, the size of the critical and caustic curves decreases and the jet image slightly contracts, while its shape is retained. On the whole, the jet image consists of individual fragments separated by the critical curves. For case (a), when moving along the jet from quadrant III upward into quadrant I until the crossing of the tangential caustic in the shape of an astroid, one image is observed (point a). When crossing the tangential caustic, two new images appear in quadrant II: one moves from the outer critical curve upward into quadrant I and the other moves from the outer critical curve downward toward the inner critical curve (points b). Subsequently, when crossing the radial critical curve in the shape of an ellipse, two additional images appear in quadrant I: one moves from the inner critical curve rightward toward the outer critical curve in quadrant IV and the other moves from the inner critical curve in quadrant I leftward toward the same curve in quadrant III (points c , d). Thus, five jet images are formed in the region within both caustics. The inverse process, i.e., the merging of the images, takes place when moving upward along the jet and crossing of the caustics. When going outside the radial and tangential caustics, respectively, three (points e) and one (point f) images remain. Four regions of significant magnification indicated by the red color appear for the specified jet configuration.

In contrast to Fig. 1a, for case (b), the radial caustic is initially crossed and two images appear in quadrant I on the inner critical curve: one moves rightward toward the outer critical curve in quadrant IV and the other moves leftward into quadrant III from the inner critical curve in quadrant I (points b). When crossing the tangential caustic, two more images appear in quadrant II: one moves from the outer critical curve upward into quadrant I and the other moves from the outer critical curve downward toward the inner critical curve (points c). Subsequently, just as in case (a), the images merge together as the jet moves outside the regions of the caustic curves.

For comparison, consider the model of a singular isothermal ellipsoid (Fig. 1c). The presence of a central singularity gives rise to a region in the source plane outside the caustic where multiple images also exist. The curve that bounds this region is called a cut (Kormann et al. 1994). When crossing this curve, an “infinitely faint” image is formed at the coordinate origin of the lens plane that moves from quadrant I toward the critical curve in quadrant IV (point a in Fig. 1c). When crossing the astroid caustic, two images appear in quadrant II: one moves from the critical curve upward into quadrant I and the other moves from the critical curve downward toward the lens center through quadrant III. Thus, four jet images (points b , c) are formed in the region within the caustic and the cut, with two images located within the critical curve having the same negative parity. When emerging from the region of the astroid caustic, the two images merge together in quadrant IV. Two images (points d , e) remain in the region outside the caustic but inside the cut. One image remains outside the latter.

As we see from Fig. 1, the images for the cases considered are quite similar, but, in contrast to an ellipsoid with a core, only two regions of high magnification (red arcs, Fig. 1c) appear in the case of a singular isothermal ellipsoid.

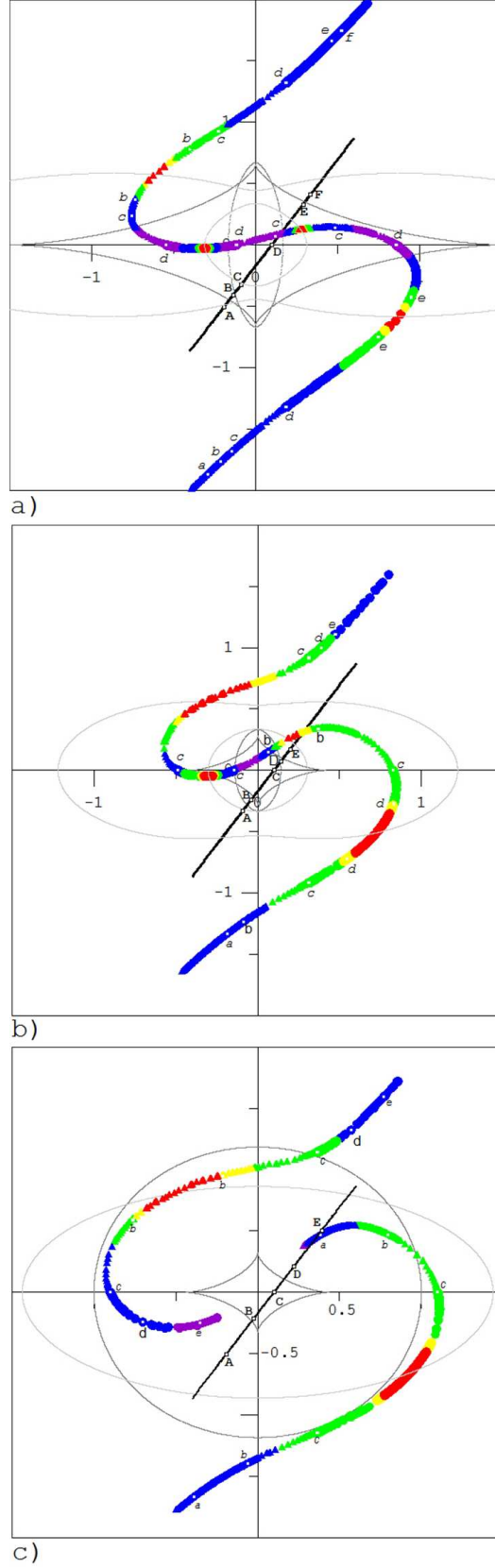


Fig. 1: Results of modeling a relativistic jet for the models of a singular ellipsoid and an ellipsoid with a core: (a) $q = 0.3$ and $s = 0.3$, (b) $q = 0.6$ and $s = 0.3$, (c) $q = 0.6$ and $s = 0.0$. The dark gray and light-gray lines indicate the caustic and critical curves, respectively; the extended jet is represented by the black line; the jet images as a function of magnification are indicated by different colors. Purple corresponds to the case when $|M| < 1$, blue - $1 < |M| < 3$, green - $3 < |M| < 7$,

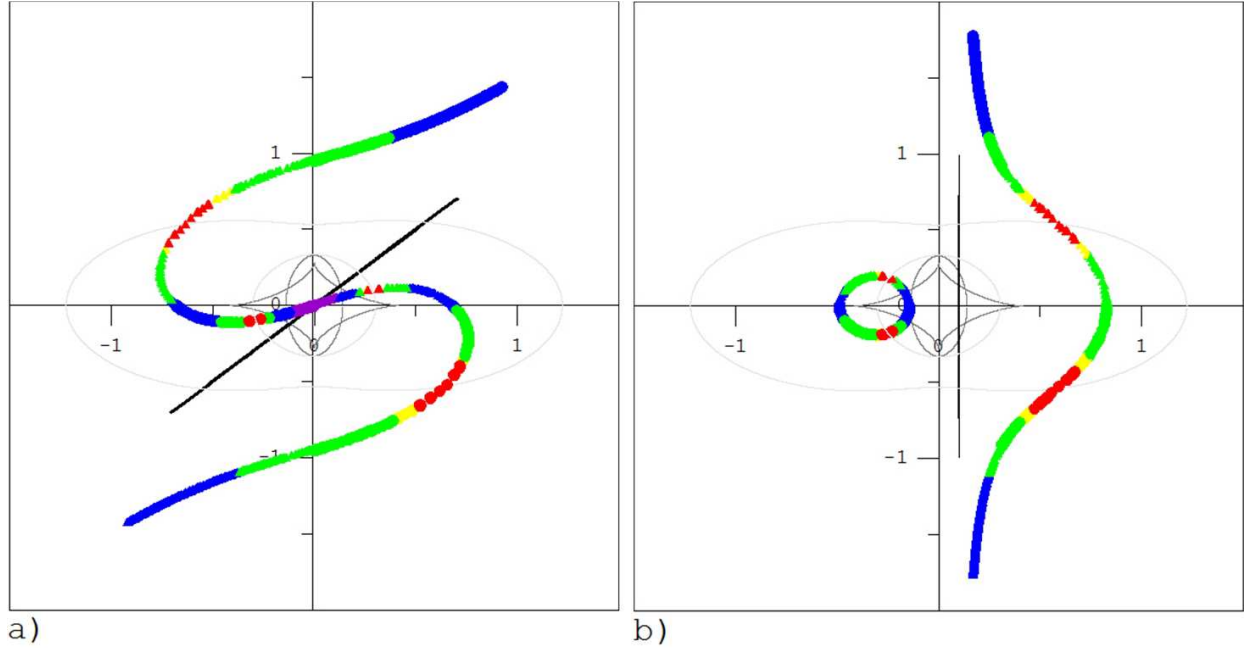


Fig. 2: Results of modeling a relativistic jet for the model of a singular ellipsoid with a core with parameters $q = 0.6$ and $s = 0.3$ at different jet inclinations to the x axis: (a) $\alpha = 45^\circ$ and the jet passes through the coordinate origin; (b) $\alpha = 90^\circ$ and the jet passes through the point (0.1, 0). The designations of the critical and caustic curves, the jet, and its images are the same as those in Fig. 1.

Let us investigate the influence of the jet inclination α on the picture of its gravitational lensing. Figure 2 shows the modeling results for an isothermal ellipsoid with a core equal to 0.3 and a spheroid axis ratio $q_3 = 0.6$ for two jet inclinations, $\alpha = 45^\circ$ (Fig. 2a) and $\alpha = 90^\circ$ (Fig. 2b). Our studies showed that for fixed parameters of the ellipsoid at jet inclinations that do not coincide with the coordinate axes (symmetry axes), the shape of the jet image is a double loop and does not change significantly with α (Figs. 1b, 2a). However, at an inclination, for example, of 90° , the shape of the jet images changes; as a result, a loop is observed in the direction of the unlensed jet and a ring about 0.3 Einstein-Chwolson radius in diameter is observed in the opposite (relative to the y axis) region. The two images that form this ring appear in quadrant II and merge together in quadrant III when crossing the ellipse caustic.

At fixed spheroid axis ratio q_3 , a change in inclination i causes a change in the axis ratio of the spheroid projection q . In the case of a singular ellipsoid, the caustic is reduced with increasing inclination and degenerates into a point at $i = 90^\circ$, implying the appearance of two jet images without bright arcs. The behavior of the caustics in the case of an isothermal ellipsoid with a core was studied in detail by Kormann et al. (1994). They showed that the caustics have different topologies, depending on the axis ratio of the ellipse projected onto the lens plane and the core radius. Thus, the shape and size of the caustics turn out to be important for the appearance of high-magnification regions, because the number of emerging images for a jet of fixed length is determined by its location relative to the caustics.

2. MODELS FOR SPIRAL GRAVITATIONAL LENS GALAXIES

2.1. Model I

When modeling the mass surface density distribution of a spiral galaxy, we will follow the approach proposed by Keeton and Kochanek (1998). We will begin our modeling with the simplest case. Consider a singular disk truncated at a characteristic distance a_d from the center and placed in an isothermal halo with a characteristic size a_h . We will call this model “model I”.

The rotation curves of spiral galaxies are the main tool for determining the mass distribution in these galaxies. According to observational data, depending on the spiral galaxy type, the rotation velocity peak for Sa, Sb, and Sc is reached approximately at 300, 220, and 175 $km\ s^{-1}$, respectively, and the rotation curve subsequently becomes flat (Sofue and Rubin 2001). No significant deviations between the rotation curves of high-redshift spiral galaxies and those of nearby spirals have been found (see, e.g., Kelson et al. 2000).

To take into account the contribution of dark matter to the rotation curve at distances $R < a_d$, we will introduce the factor f_d . The equality of f_d to one implies that the rotation curve is entirely determined by the visible disk component. It should be noted that analysis of the disk surface densities obtained by different methods showed that the disk does not contain a large amount of dark matter (Holmberg and Flynn 2004). Here, this factor was taken to be $f_d = 0.85$ (Sackett 1997).

The lensing potential for model I, the lens equation, and the expressions for the image magnification are given in the Appendix.

To model the jet images produced by gravitational lensing for the potential of model I, we will fix the following model parameters:

f_d	0.85
a_h	$0.8a_d$
q_{3h}	0.8

The choice of the parameters is dictated by two main criteria: the halo shape is nearly spherical (Dehnen and Binney 1998) and the rotation curve of a spiral galaxy is flat. At fixed jet parameters, different caustic and cut geometries and, as a result, different image geometries are observed depending on q_d and a_d . In Fig. 3, except for the case of $q_d = 0.01$ and $a_d = 100.0$ (Fig. 3b) that corresponds to a “disk geometry”, the relativistic jet crosses the caustic. As the caustic curve is approached, the images with different parities approach each other, merging together when crossing the caustic. This is characterized by the appearance of bright extended arcs. In the case of a disk geometry, the caustic “pierces” the cut and pairwise symmetric images appear; the central images are faint, while the brighter images are separated by a considerable distance (of the order of four Einstein-Chwolson radii). Note that as yet no such case has been encountered in observations (see, e.g., the CASTLES

catalog¹), which probably suggests that the halo should be taken into account for spiral lens galaxies. Based on model I, let us investigate the influence of the inclination of the spheroids that describe the disk and halo. For $q_{3d} = 0.05$ and $a_d = 1.0$, Fig. 4 shows the jet lensing for coaxial spheroids and inclinations i of 0° , 30° , and 45° . Note that the choice of the above values for q_{3d} and a_d is dictated by the Milky Way parameters (see, e.g., Grimm et al. 2002). The mean axis ratio of spiral galaxies is $\sim 0.1 - 0.2$ (de Grijs and van der Kruit 1996). However, a change in q_{3d} from 0.05 to 0.1 has no significant effect on the shape of the jet images at other identical model and jet parameters. We see from the figure that as the inclination increases, the caustic (astroid) is reduced and the shape of the images changes. As with the model of a singular isothermal ellipsoid, the caustic degenerates into a point when 90° is reached.

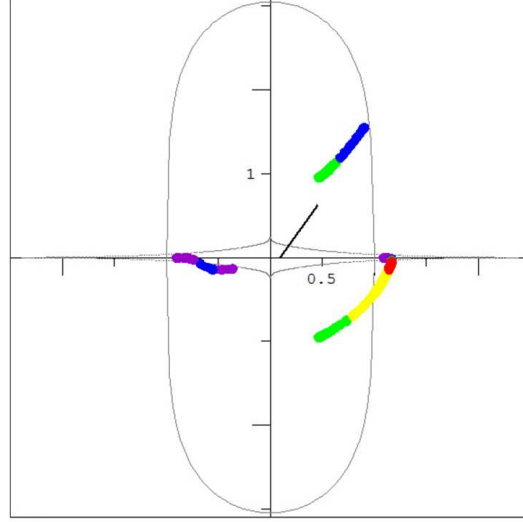
The expression for the galactic rotation curve in model I is given in the Appendix (Eq. A21), while the shape of the curve itself with disk parameters $q_{3d} = 0.05$ and $a_d = 1.0$ is shown in Fig. 5a. We see from the figure that the rotation curve in this model at small R , i.e., near the galactic center, does not correspond to the observed rotation curves of spiral galaxies (Sofue and Rubin 2001).

To compare the modeling results obtained for model I with the complicated models considered below, we will use the approach described in Section 1 of this paper. For the disk parameters considered above, we will choose such a length of the jet that it crosses both the caustic and the cut twice (Fig. 6a). A jet with $\alpha = 60^\circ$ crosses the x axis at a point of 0.1 Einstein-Chwolson radius. All designations in Fig. 6 are the same as those in Fig. 1. The shape of the images, except for some features, and their behavior for model I are similar to those in the case of a singular isothermal ellipsoid, but the critical curves differ significantly (Fig. 6a).

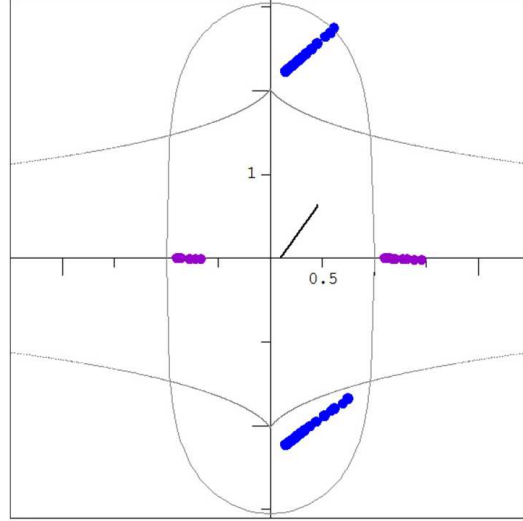
2.2. Model II

Consider the more realistic model of a spiral galaxy that is a galactic disk approximated by a Kuzmin disk (Eqs. A23 and A24) embedded in a halo modeled by a nonsingular isothermal ellipsoid. We will call this model “model II”. The lensing potential for this model, the lens equation, and the expression for the image magnification are given in the Appendix. The model under consideration is described by the following parameters: the characteristic disk, a_d , and halo, a_h , sizes, the axis ratios in the disk q_{3d} and halo q_{3h} , and the disk mass m_d . These parameters were determined from the following conditions: (i) the rotation curve characteristic of spirals, (ii) the specified Galactic rotation velocity of the Sun $V_0(8.0 \text{ kpc}) = 235 \text{ km s}^{-1}$ (Reid and Brunthaler 2004), and (iii) the local disk surface density in the solar neighborhood $\Sigma_\odot = 75 \pm 25 \text{ } M_\odot \text{ pc}^{-2}$. They are given below:

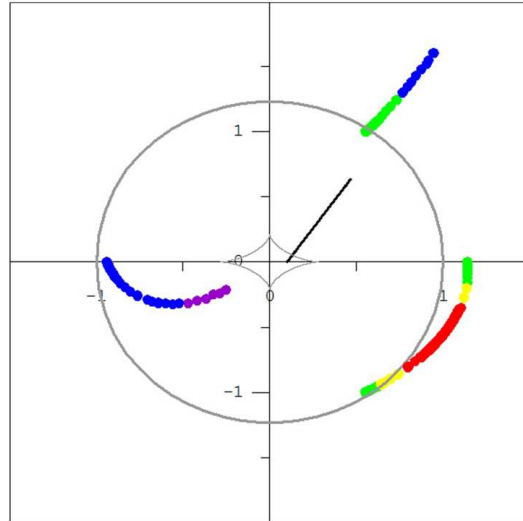
¹<http://www.cfa.harvard.edu/castles/noimages.html>



a)



b)



c)

Fig. 3: Results of modeling a relativistic jet for model I at $i = 0^\circ$: (a) $q_{3d} = 0.01$ and $a_d = 1.0$; (b) $q_{3d} = 0.01$ and $a_d = 100.0$; (c) $q_{3d} = 0.5$ and $a_d = 1.0$. The designations are the same as those in Fig. 1.

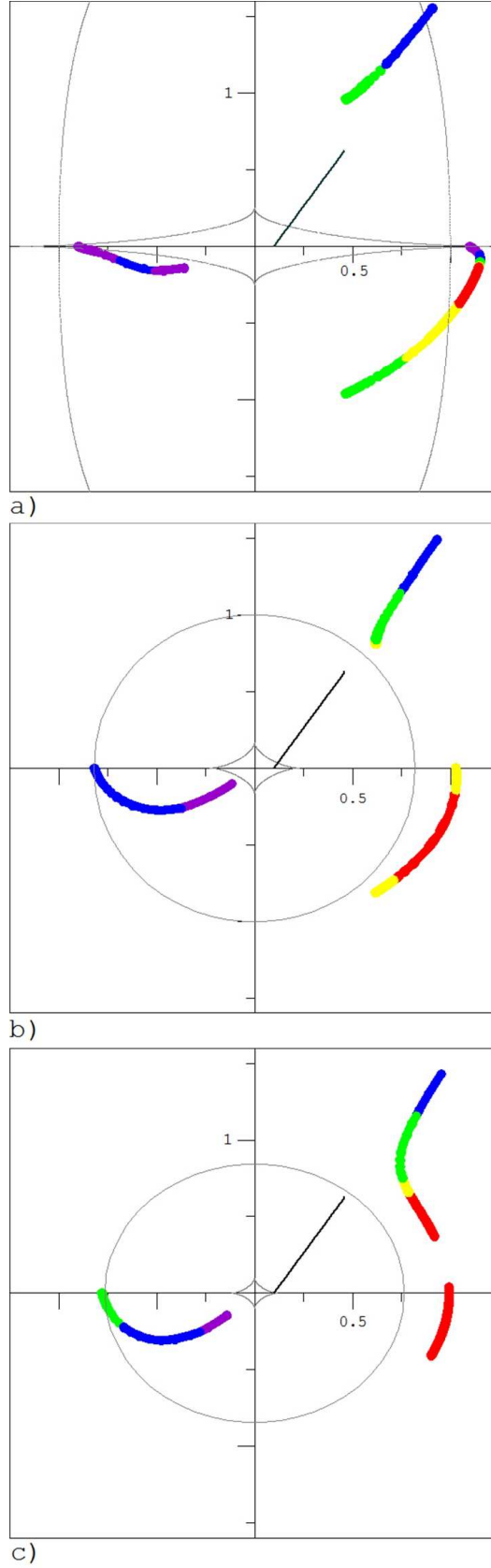


Fig. 4: Results of modeling a relativistic jet at various inclinations i for model I with $q_{3d} = 0.05$ and $a_d = 1.0$; (a) $i = 0^\circ$; (b) $i = 30^\circ$, (c) $i = 45^\circ$. The designations are the same as those in Fig. 1.

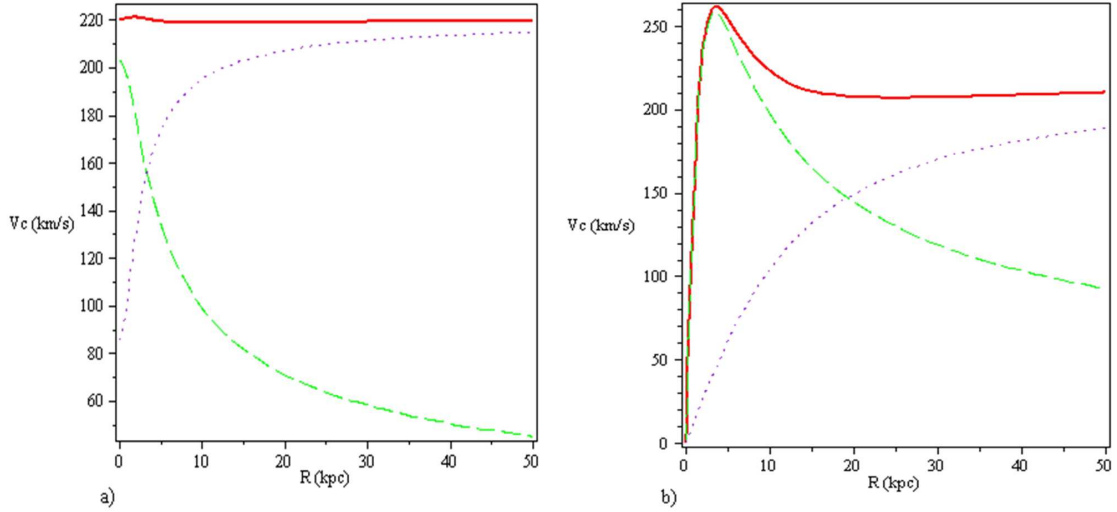


Fig. 5: Rotation curves for models I(a) and II (b) calculated for $q_d = 0.05$ and $a_d = 1.0$. The red solid, green dashed, and purple dotted lines indicate the total rotation curve, the disk contribution, and the halo contribution, respectively.

$a_d = 1.0$ $m_d = 1.0 \cdot 10^{11} M_\odot$ $q_{3h} = 0.8$	q_{3d}	a_h
	0.01	4.63
	0.05	4.36
	0.10	4.07
	0.15	3.83

Figure 5b for $q_{3d} = 0.05$ and $a_d = 1.0$ shows the rotation curve for model II in comparison with model I.

It should be noted that a Kuzmin disk approximates better the galactic disk than a nonsingular isothermal ellipsoid, because, in this case, the rotation curve coincides in shape with the rotation curves observed for spiral galaxies.

Radial and tangential caustics appear for typical q_{3d} of spiral galaxies in model II; in contrast to the previously considered models of the mass distribution in the lens, part of the astroid lies outside the radial caustic. The caustic curves of this type are called “naked cusps”. Figure 6b presents the jet modeling results in model II for the same galactic disk parameters as those in model I. The shape of the emerging images and their behavior are similar to those in the case of a nonsingular isothermal ellipsoid, but the critical curves are different. The number of emerging regions of enhanced brightness is twice that in model I. This corresponds to four crossings of the critical curves, although the extent of these regions is considerably smaller.

2.3. Model III

Let us investigate the question of whether the bulge in the spiral galaxy structure should be taken into account when considering the gravitational lensing of a jet by adding a bulge

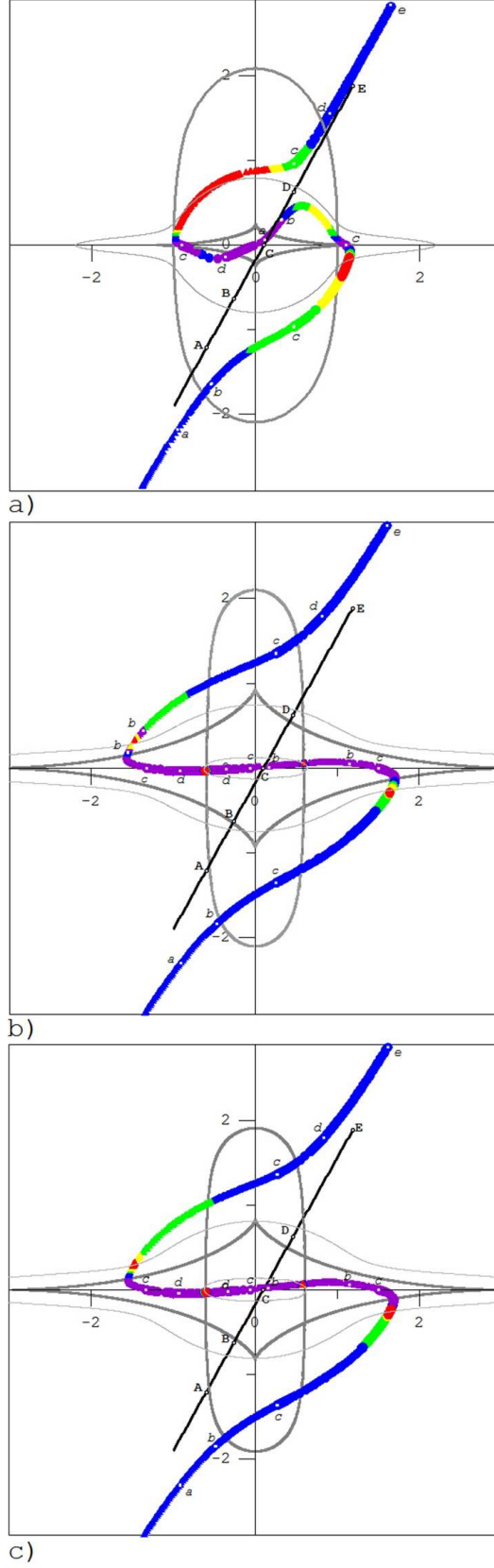


Fig. 6: Comparison of the results of modeling a relativistic jet for models I, II, and III. The jet geometry ($\alpha = 60^\circ$) and model parameters ($q_{3d} = 0.05$ and $a_d = 1.0$) are fixed; (a) for model I, (b) for model II, and (c) for model III. The designations of the critical and caustic curves, the jet, and its images are the same as those in Fig. 1.

in the shape of a Kuzmin disk to model II (model III, Eq. A30).

We determine the model parameters from the condition that the rotation curves for models II and III coincide for given q_{3d} . In the model, we chose the bulge axis ratio $q_{3b} = 0.6$ and the characteristic core radius $a_b = 0.8$ (Dehnen and Binney 1998). The fixed parameters of model II are given below:

$a_d = 1.0$	q_{3d}	$m_b, 10^{10} M_\odot$	a_h
$m_d = 8.8 \cdot 10^{10} M_\odot$	0.01	1.37	4.68
$q_{3h} = 0.8$	0.05	1.36	4.42
$q_{3b} = 0.6$	0.10	1.34	4.13
$a_b = 0.8$	0.15	1.32	3.88

Figure 6c presents the jet modeling results for model III in comparison with models I and II (Figs. 6a, 6b). The shape of the emerging images, their behavior, and the critical and caustic curves in models II and III are essentially identical, suggesting that the bulge introduces no significant change in the picture of gravitational lensing of the jet for the chosen model parameters.

Note that all three galactic components are assumed to be coaxial, although, according to observations, this condition is not met for the bulge. Our studies for noncoaxial components showed that the modeling results obtained in this case differ only slightly from those for coaxial ones. For example, if the angle between the disk and halo symmetry axes is 45° and between the disk and bulge in model III is 20° , then the maximum displacement of the jet image compared to that for coaxial galactic components in models II and III is only 0.05 Einstein-Chwolson radius. For model I, Fig. 7 shows the jet images for the coaxial and noncoaxial cases. We see from this figure that the shape of the images does not change significantly, but only a slight displacement, whose maximum value does not exceed ~ 0.1 Einstein-Chwolson radius, takes place. It should be noted that when the jet crosses the caustic curve near the cusp, the maximum displacement can reach ~ 0.2 Einstein-Chwolson radius.

3. THE COUNTERJET

For a given mass surface density distribution in the lens galaxy, the observed shape and relative positions of the images in the plane of the sky are determined by the position of the initial point and the jet length and inclination relative to the caustic curves. Different configurations of jet images both in their number and parity and in magnification at each image point and the presence of bright extended arcs can be obtained by changing these parameters for a specific model of the lens galaxy. The gravitational lensing of relativistic jets can, in principle, allow the counterjet that cannot be observed in the absence of gravitational lensing due to the geometry to be observed. This, in turn, can be a test for the generation models of relativistic jets when discussing the question of whether such a counterjet is present or absent. Based on the lens models considered, we investigated the question of how the counterjet would manifest itself during gravitational lensing. It turned out that a great

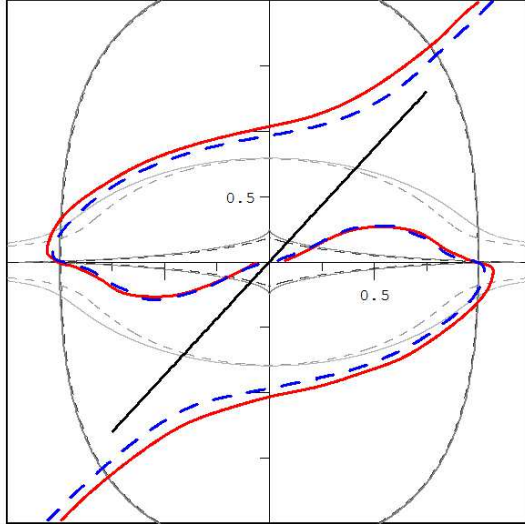


Fig. 7: Results of modeling the images of a relativistic jet for model I in the case of coaxial components (red solid thick line) and noncoaxial components (blue dashed thick line), when the angle between the disk and halo symmetry axes is 45° . The corresponding caustic and critical curves are indicated by the thin solid and dashed lines. The jet inclination (indicated by the black color) is $\alpha = 60^\circ$; the model parameters are $q_{3d} = 0.05$ and $a_d = 1.0$.

variety of lensing pictures, including extended arcs and almost circumferences (under the caustic curve crossing condition), could be formed by changing its length and direction. For ringlike jet images consisting of bright extended arcs to appear, the jet must cross the tangential caustic almost along the tangent to its cusps.

A characteristic example of the appearance of such a ringlike structure is shown in Fig. 8 for model I. The initial point of the jet marked by the asterisk lies outside the tangential caustic and is inclined at the angle $\alpha = 60^\circ$ to the x axis (as in the previously considered cases); the remaining parameters of the chosen model are $q_{3d} = 0.05$, $a_d = 1.0$, and $i = 30^\circ$.

4. B0218+357

Based on the results of the above modeling, we can assume that some of the observed gravitationally lensed systems with large-scale rings can be explained by the lensing of their jets. It may well be that the source B0218+357, in which two compact core images and an extended ring structure are observed in the radio band, is such an object. In particular, 5-GHz MERLIN observations of this source showed that the ring structure consists of two arcs each of which, in turn, breaks up into several separate regions of enhanced brightness (Biggs et al. 2001).

An attempt to model the lens mass distribution in the system B0218+357 was made by Wucknitz et al. (2004). As the model that described most adequately the observed picture, the authors used a singular isothermal elliptical power-law lensing potential specified by the

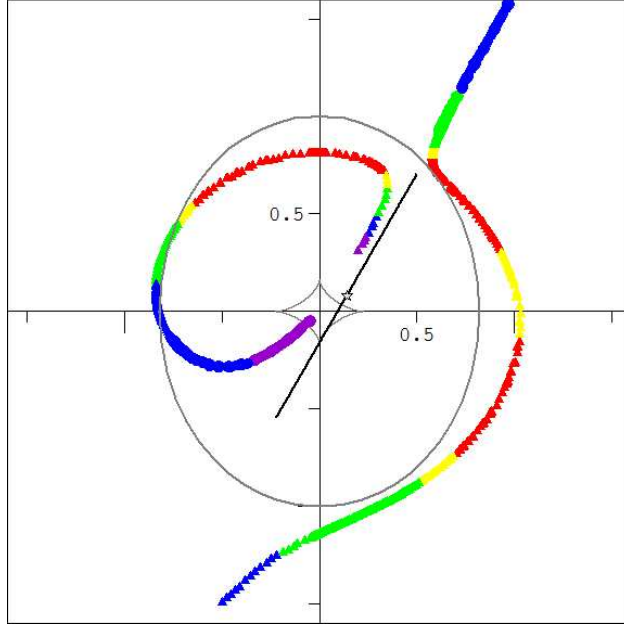


Fig. 8: Results of modeling a relativistic jet and counterjet for model I at $i = 30^\circ$, $q_{3d} = 0.05$, and $a_d = 1.0$. The initial point of the jet designated by the asterisk is located outside the astroid and has coordinates (0.14, 0.08) in the lens plane. The designations are the same as those in Fig. 1.

formula

$$\psi(x, y) = \theta_0 \sqrt{\frac{x^2}{(1 + \epsilon)^2} + \frac{y^2}{(1 - \epsilon)^2}}, \quad (2)$$

where θ_0 is the Einstein-Chwolson angle and ϵ is the ellipticity of the distribution.

According to VLA data, the large-scale jet is inclined with respect to the line connecting the source's two images A and B at the angle ϖ that has not been determined accurately, but, judging by its VLA images at 8.4 GHz (Fig. 4 in Biggs et al. 2003), it is approximately equal to 75° ; the image intensity ratio is $F_A/F_B \simeq 2.2 - 3.9$, depending on frequency (see Table 3 in Mittal et al. 2006). If, based on the model proposed by Wucknitz et al. (2004), we direct the jet precisely at this angle, then its images will be dim, slightly curved lines that are hard to associate with a ring. The following question arises: Can a ringlike structure still be obtained in this model and what is needed for this? As was pointed out above, bright arclike structures appear when the jet approaches the caustics (or when it crosses them). In the case of Wucknitz's model, a counterjet that will cross the tangential caustic (astroid) is needed to obtain such a structure. However, in this case, the jet itself must be directed at an angle $\varpi \simeq 30^\circ$ and the counterjet length must be comparable to the Einstein-Chwolson radius, which is actually not observed.

An interesting question is whether the parameters and the position of the initial point of the jet can be chosen within the framework of models I-III considered here to explain the observed geometry of B0218+357, including its large-scale structure consisting of two extended arcs. Our study showed that different sets of parameters that allow the observed geometry of the system and the intensity ratio of the emerging images to be obtained in the

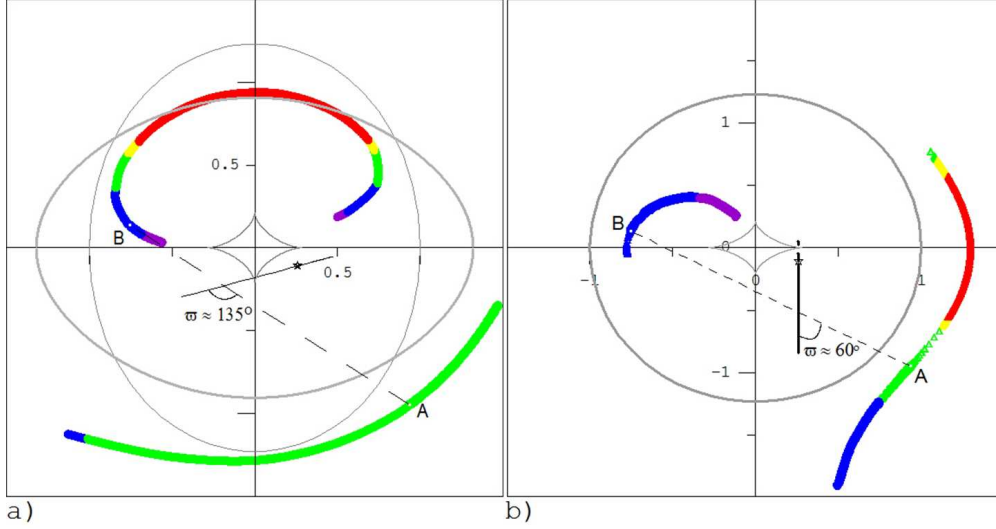


Fig. 9: Results of modeling a relativistic jet for model I at $q_d = 0.5$ and $a_d = 1.0$ for the gravitational lensing of B0218+357. The initial point of the jet that corresponds to the position of the source’s compact core has coordinates $(0.26, -0.11)$ in the lens plane. Panel (a) illustrates the situation where the jet is directed at an angle $\varpi \simeq 135^\circ$ with respect to the line connecting images A and B and crosses the lower edge of the tangential caustic; in panel (b), the jet is directed at an angle $\varpi \simeq 60^\circ$ and has a counterjet with a length approximately equal to one fifth of the Einstein-Chwolson radius that crosses the right end of the astroid. The designations are the same as those in Figs. 1 and 6.

models considered (see above). However, obtaining bright extended arcs is very nontrivial and is possible by no means in all cases. As one of such realizations, we can choose model I with a characteristic disk size $a_d = 1.0$ and an axis ratio of its projected surface density ellipse $q_d = 0.5$. If we place the initial point of the jet at the point with coordinates $(0.26, -0.11)$, then the distance between the images of the compact core is $\simeq 335$ mas and the magnification ratio of its images is $\simeq 3.3$, in good agreement with observational data (Biggs et al. 1999; Patnaik et al. 1993). Bright semiring structures (arcs) in this model appear at an angle $\varpi \simeq 135^\circ$ and no counterjet is required in this case (Fig. 9a). It should be noted that the angle between the jet and the line connecting the images for the chosen parameters differs significantly from the observed one. If we direct the jet at an angle $\varpi \simeq 60^\circ$ for the same model parameters and add the counterjet, then we will obtain the caustic crossing and bright arcs, as is illustrated in Fig. 9b. In this case, the angle ϖ is fairly close to the observed one and the counterjet length accounts for less than one fifth of the Einstein-Chwolson radius. In addition, multifrequency VLBI observations at 1.65 GHz revealed a component in image A in the direction opposite to that of the component associated on small scales with the jet relative to the compact core that can be associated with the counterjet (Mittal et al. 2006). At the same time, this component is not observed in image B, which is explained in terms of the models considered by the fact that the fainter image B and the corresponding image of the jet are spatially more “compressed” than the brighter image A (see, e.g., Fig. 9b).

5. CONCLUSIONS

We modeled the images of relativistic jets from extragalactic sources produced by gravitational lensing by galaxies of various types. To describe the surface density distribution for elliptical lens galaxies, we used the models of a singular isothermal ellipsoid and an ellipsoid with a core; for spiral lens galaxies, we considered the model of a disk and a softened disk embedded by a singular isothermal dark matter halo, the Kuzmin model of a disk in an isothermal halo, and the model of a disk and a bulge in an isothermal halo. The critical and caustic curves and the relativistic jet images for the three multicomponent models of spiral galaxies presented here were compared with one another. For the chosen parameters, the shape of the emerging images, their behavior, and the critical and caustic curves are almost identical for models II and III. This suggests that including a low mass bulge similar to the Milky Way bulge introduces no significant changes in the picture of gravitational lensing of the jet.

We showed that the observed large-scale ring structures could be produced by the gravitational lensing of relativistic jets by galaxies for certain relative positions of the jet and the caustic curves. In particular, for extended bright arcs to appear in the models considered here, the jet must cross twice the tangential caustic almost along the tangent to its cusps.

For the gravitationally lensed system B0218+357, we compared the model used previously to determine the Hubble constant (Wucknitz et al. 2004) with the models of the mass surface density distribution in a spiral lens galaxy proposed here. For example, in the model with a singular elliptical power-law potential mentioned above, it is highly problematic to obtain jet images in the shape of a ring structure for the observed (outside the lensing region) direction of the large-scale relativistic jet relative to the compact core images. The models being discussed here that allow for the gravitational lensing of a large-scale jet give an image of the system B0218+357 that, on the whole, closer to the observed one.

In view of its “isolated” spatial location and the measured time delay between its images, the system B0218+357 is well suitable for an independent determination of the Hubble constant. However, apart from the time delay, this requires an accurate knowledge of the system’s geometry, in particular, the relative positions of the lens galaxy and the emission source. Deep optical HST observations of B0218+357 aimed at determining the position of the lens galaxy, along with the use of the model by Wucknitz et al. (2004), allowed the Hubble constant to be estimated, which changes depending on the assumptions of the authors regarding the spiral arms of the lens galaxy (York et al. 2005). Since the distance between the images of the compact core for the source under consideration in the radio band is fairly small, $\simeq 335$ mas, (it is slightly smaller in the optical band) and since the lens is a spiral galaxy, optical observations are very complicated. Submillimeter observations are preferred for determining the position of the lens galaxy due to the emission of cold dust in its spiral arms. However, the resolution of present-day observatories in this band is not yet sufficient, which makes the direct determination of accurate relative positions of the lens and the source in the immediate future problematic. Therefore, to reconstruct the geometry of a gravitationally lensed system, modeling remains topical. As was noted above, the Hubble

constant H determined in the model also depends on the relative positions of the lens and the source. For example, Wucknitz et al. (2004) provided $H \simeq 78 \text{ km s}^{-1} \text{ Mpc}^{-1}$, while York et al. (2005) gave 70 and $61 \text{ km s}^{-1} \text{ Mpc}^{-1}$, depending on the method of determining the lens position. A significant difference of the relative spatial positions of the lens and the source in the models proposed here from those obtained by other authors and between themselves leads to a considerable variety in the estimates of the Hubble constant, $H \simeq 35\text{--}90 \text{ km s}^{-1} \text{ Mpc}^{-1}$.

As another possible astrophysical application of our results, we will note the possibility of measuring the propagation velocity of jet knots during the observation of its gravitationally lensed images. This possibility follows from the following considerations. In the models considered here, first, the lensed jet image located outside the Einstein-Chwolson radius is always “extended” compared to the jet projection onto the lens plane. Second, when the jet crosses the caustic, the sizes of the emerging bright arc exceed the initial sizes of the jet projection by many times. These peculiarities make it possible to calculate the jet propagation velocity by measuring the displacements of individual bright knots in the images with time. However, such studies are a separate independent problem and are beyond the scope of this paper.

6. ACKNOWLEDGMENTS

This work was supported by the “Origin, Structure, and Evolution of Objects in the Universe” Program of the Presidium of the Russian Academy of Sciences, the Program for Support of Leading Scientific Schools (project no. NSh-5069.2010.2), and the State contract P1336. We are also grateful to the referees for a careful reading of the paper and helpful remarks.

7. APPENDIX

All of the dimensional variables, including the variables x and y and the parameter s , were normalized to the Einstein-Chwolson radius. The Einstein-Chwolson radius is a characteristic lensing scale in the lens plane. For axisymmetric lens models, it is defined by the formula

$$\xi_0 = \sqrt{\frac{4Gm}{c^2} \frac{D_d D_{ds}}{D_s}}, \quad (\text{A1})$$

where m is the lens mass, D_d and D_s are the distances from the observer to the lens and the source, respectively, and $D_{ds} = D_s - D_d$ is the distance between the source and the lens.

The lens equation is

$$\begin{cases} X &= x - \Phi_x \\ Y &= y - \Phi_y \end{cases} \quad (\text{A2})$$

where (X, Y) specify the jet points, Φ_x and Φ_y are the first derivatives of the lensing potential Φ .

The image magnification is

$$M^{-1} = 1 - \Delta\Phi + \Phi_{xx}\Phi_{yy} - \Phi_{xy}^2, \quad (\text{A3})$$

where $\Phi_{xx}, \Phi_{yy}, \Phi_{xy}$ are the second derivatives of the lensing potential Φ .

For a multicomponent lens model, the lensing potential is the sum of the potentials of its individual components, $\Phi = \sum \phi_i$. Accordingly, the derivative of the potential Φ - is the sum of the derivatives of the potentials ϕ_i :

$$\Phi_{x(y)} = \sum \phi_{ix(y)}. \quad (\text{A4})$$

A Singular Isothermal Ellipsoid and an Ellipsoid with a Core

The lensing potential, i.e. the projection of the three-dimensional potential onto the lens plane, is defined by the formula

$$\phi(s, q) = x\alpha_x + y\alpha_y - \frac{1}{2}bs \ln[(\psi + s)^2 + (1 - q^2)x^2], \quad (\text{A5})$$

$$\begin{aligned} \alpha_x &= \frac{b}{\sqrt{1 - q^2}} \arctan \frac{\sqrt{1 - q^2}x}{\psi + s}, \\ \alpha_y &= \frac{b}{\sqrt{1 - q^2}} \operatorname{arth} \frac{\sqrt{1 - q^2}y}{\psi + q^2s}, \end{aligned} \quad (\text{A6})$$

where $e = \sqrt{1 - q^2}$, $b = e / \arcsin(e)$, $\psi = \sqrt{q^2(s^2 + x^2) + y^2}$.

The first derivatives of the potential $\phi(s, q)$ are

$$\begin{aligned} \phi(s, q)_x &= \alpha_x + bx \frac{\psi - \frac{q^2(x^2+s^2)}{\psi}}{Z_1} - b \frac{\frac{q^2xy^2}{\psi}}{Z_2}, \\ \phi(s, q)_y &= \alpha_y - b \frac{sy + \frac{y(x^2+s^2)}{\psi}}{Z_1} + by \frac{\psi + q^2s - \frac{y^2}{\psi}}{Z_2}, \\ Z_1 &= (\psi + s)^2 + (1 - q^2)x^2, \\ Z_2 &= (\psi + q^2s)^2 - (1 - q^2)y^2. \end{aligned} \quad (\text{A7})$$

The second derivatives of the potential $\phi(s, q)$ are

1)

$$\phi_{xx}(s, q) = \alpha_{x,x} + W_{1x} + W_{2x}, \quad (\text{A8})$$

where

$$\alpha_{x,x} = b \frac{\psi + s - \frac{q^2x^2}{\psi}}{Z_1}; \quad (\text{A9})$$

$$W_{1x} = \frac{b}{Z_1} \left(\psi - \frac{q^2(s^2 + 2x^2)}{\psi} + \frac{q^4 x^2 (x^2 + s^2)}{\psi^3} \right) + \frac{2bx^2}{Z_1^2} \left(-\psi + \frac{q^2 x^2}{\psi} + \frac{q^2 s^2}{\psi} - q^2 s + \frac{q^4 s x^2}{\psi^2} + \frac{q^4 s^3}{\psi^2} \right); \quad (\text{A10})$$

$$W_{2x} = -\frac{bq^2 y^2}{Z_2} \left(\frac{1}{\psi} - \frac{q^2 x^2}{\psi^3} \right) + \frac{bq^4 y^2}{Z_2^2} \frac{2x^2(\psi + q^2 s)}{\psi^2}; \quad (\text{A11})$$

$$Z_1 = (\psi + s)^2 + (1 - q^2)x^2, Z_2 = (\psi + q^2 s)^2 - (1 - q^2)y^2. \quad (\text{A12})$$

2)

$$\phi_{yy}(s, q) = \alpha_{y,y} + U_{1y} + U_{2y}, \quad (\text{A13})$$

where

$$\alpha_{y,y} = b \frac{\psi + q^2 s - \frac{y^2}{\psi}}{Z_2}; \quad (\text{A14})$$

$$U_{1y} = -\frac{b}{Z_1} \left(\frac{x^2 + s^2}{\psi} + s - \frac{(x^2 + s^2)y^2}{\psi^3} \right) + \frac{2(\psi + s)y^2 b}{\psi Z_1^2} \left(\frac{x^2 + s^2}{\psi} + s \right); \quad (\text{A15})$$

$$U_{2y} = \frac{b}{Z_2} \left(\psi + q^2 s - \frac{2y^2}{\psi} + \frac{y^4}{\psi^3} \right) - \frac{2bq^2 y^2 (\psi + s)}{Z_2^2} \left(1 + \frac{q^2 s}{\psi} - \frac{y^2}{\psi^2} \right). \quad (\text{A16})$$

3)

$$\phi_{xy}(s, q) = \alpha_{x,y} + W_{1y} + W_{2y}, \quad (\text{A17})$$

where

$$\alpha_{x,y} = -b \frac{xy}{\psi Z_1} \quad (\text{A18})$$

$$W_{1y} = \frac{bxy}{Z_1} \left(\frac{1}{\psi} + \frac{q^2(x^2 + s^2)}{\psi^3} \right) - \frac{2bxy(\psi + s)}{Z_1^2 \psi} \left(\psi - \frac{q^2(x^2 + s^2)}{\psi} \right); \quad (\text{A19})$$

$$W_{2y} = -\frac{bq^2 xy}{Z_2 \psi} \left(2 - \frac{y^2}{\psi^2} \right) + 2 \frac{bq^4 xy^3 (\psi + s)}{Z_2^2 \psi^2}. \quad (\text{A20})$$

The circular velocity in the symmetry plane of an isothermal spheroid is defined by the formula

$$V_c^2(R) = V_c^2 \left(1 - \frac{e}{\arcsin(e)} \frac{s}{\sqrt{R^2 + e^2 s^2}} \arctan \left[\frac{\sqrt{R^2 + e^2 s^2}}{q_3 s} \right] \right). \quad (\text{A21})$$

Model I

The lensing potential for model I is

$$\Phi_I = f_d \{ \phi(0, q_d) - \phi(a_d, q_d) + \phi(a_h, q_h) \} + (1 - f_d) \phi(0, q_h), \quad (\text{A22})$$

where $\phi(0, q_d)$ and $\phi(0, q_h)$ are the potentials for a singular isothermal ellipsoid with axis ratios q_d and q_h , respectively, $\phi(a_d, q_d)$ and $\phi(a_h, q_h)$ are the potentials of an isothermal ellipsoid with cores $s = a_d$ and $s = a_h$ and axis ratios q_d and q_h , respectively.

The first and second derivatives of the potential Φ_I can be calculated from Eqs. (A7)-(A20) using (A4).

Model II

The lensing potential for model II is

$$\Phi_{II} = \phi_k(a_d, q_d) + \phi(a_h, q_h), \quad (\text{A23})$$

where

$$\phi_k(s, q) = \frac{1}{2} b_k^2 \ln[(\psi + s)^2 + (1 - q^2)x^2] \quad (\text{A24})$$

is the potential of a Kuzmin disk, $\phi(a_h, q_h)$ is the potential of an isothermal ellipsoid with a core a_h and an axis ratio q_h .

b_k is the normalization factor that can be determined from the relation $m_d = \pi b_k^2 \Sigma_{cr}$, where m_d is the disk mass, $\Sigma_{cr} = \frac{c^2 D_s}{4\pi G D_d D_{ds}}$ is the critical density, a_d is the characteristic disk scale normalized to the Einstein-Chwolson radius.

The derivatives of the Kuzmin disk potential $\phi_k(s, q)$ are

$$\phi_k(s, q)_x = \frac{b_k^2 x}{Z_1} L_1, \quad (\text{A25})$$

where $L_1 = \frac{\psi + q^2 s}{\psi}$.

$$\phi_k(s, q)_y = \frac{b_k^2 y}{Z_1} L_2, \quad (\text{A26})$$

where $L_2 = \frac{\psi + s}{\psi}$.

$$\phi_k(s, q)_{xx} = \frac{b_k^2}{Z_1} \left(L_1 - \frac{q^4 s x^2}{\psi^3} - 2 \frac{x^2}{Z_1} L_1^2 \right) \quad (\text{A27})$$

$$\phi_k(s, q)_{yy} = \frac{b_k^2}{Z_1} \left(L_2 - \frac{s y^2}{\psi^3} - 2 \frac{y^2}{Z_1} L_2^2 \right) \quad (\text{A28})$$

$$\phi_k(s, q)_{xy} = -\frac{b_k^2 x y}{Z_1} \left(\frac{q^2 s}{\psi^3} + \frac{2}{Z_1} L_1 L_2 \right) \quad (\text{A29})$$

Model III

The lensing potential for model III is defined by the formula

$$\Phi_{III} = \phi_k(a_d, q_d) + \phi_k(a_b, q_b) + \phi(a_h, q_h), \quad (\text{A30})$$

where $\phi_k(a_d, q_d)$ и $\phi_k(a_b, q_b)$ are the potentials of a Kuzmin disk with cores $s = a_d$ и $s = a_b$ and axis ratios q_d and q_b , respectively, $\phi(a_h, q_h)$ is the potential of an isothermal ellipsoid with a core a_h and axis ratios q_h .

REFERENCES

1. A. D. Biggs, I. W. A. Browne, P. Helbig, et al., *Mon. Not. R. Astron. Soc.* 304, 349 (1999).
2. A. D. Biggs, I. W. A. Browne, P. N. Wilkinson, et al., *ASP Conf. Ser.* 304, 137 (2001).
3. A. D. Biggs, O. Wucknitz, R. W. Porcas, et al., *Mon. Not. R. Astron. Soc.* 338, 599 (2003).
4. I. W. A. Browne, A. R. Patnaik, D. Walsh, and P. N. Wilkinson, *Mon. Not. R. Astron. Soc.* 263, L32 (1993).
5. A. S. Cohen, J. N. Hewitt, C. B. Moore, and D. B. Haarsma, *Astrophys. J.* 545, 578 (2000).
6. W. Dehnen and J. Binney, *Mon. Not. R. Astron. Soc.* 294, 429 (1998).
7. C. Feron, J. Hjorth, J. P. McKean, and J. Samsing, *Astrophys. J.* 696, 1319 (2009).
8. R. de Grijs and P. C. van der Kruit, *Astron. Astrophys. Suppl. Ser.* 117, 19 (1996).
9. H. J. Grimm, M. Gilfanov, and R. Sunyaev, *Astron. Astrophys.* 391, 923 (2002).
10. J. N. Hewitt, E. L. Turner, D. P. Schneider, et al., *Nature* 333, 537 (1988).
11. J. Holmberg and C. Flynn, *Mon. Not. R. Astron. Soc.* 352, 440 (2004).
12. A. Kassiola and I. Kovner, *Astrophys. J.* 417, 450 (1993).
13. C. R. Keeton and C. S. Kochanek, *Astrophys. J.* 495, 157 (1998).
14. D. D. Kelson, G. D. Illingworth, P. G. van Dokkum, and M. Franx, *Astrophys. J.* 531, 159 (2000).
15. I. R. King, *An Introduction to Classical Stellar Dynamics* (Univ. of California, Berkeley, 1994; Editorial URSS, Moscow, 2002).
16. R. Kormann, P. Schneider, and M. Bartelmann, *Astron. Astrophys.* 284, 285 (1994).
17. G. G. Kuzmin, *Astron. Zh.* 33, 27 (1956).
18. R. Mittal, R. Porcas, O. Wucknitz, et al., *Astron. Astrophys.* 447, 515 (2006).
19. S. Nair, D. Narasimha, and A. P. Rao, *Astrophys. J.* 407, 46 (1993).
20. R. Narayan and M. Bartelmann, *astro-ph/9606001v2* (1997).
21. A. Patnaik, I. Browne, L. King, et al., *Mon. Not. R. Astron. Soc.* 261, 435 (1993).
22. A. R. Patnaik, R. W. Porcas, and W. A. Browne, *Mon. Not. R. Astron. Soc.* 274, L5 (1995).
23. H. J. Reid and A. Brunthaler, *Astrophys. J.* 616, 872 (2004).
24. P. D. Sackett, *Astrophys. J.* 483, 103 (1997).
25. M. Schmidt, *Bull. Astron. Inst. Netherlands* 13, 15 (1956).

26. P. Schneider, J. Ehlers, and E. E. Falco, Gravitational Lenses, 2nd ed. (Springer, Berlin, Heidelberg, New York, Barcelona, Hong Kong, London, Milan, Paris, Singapore, Tokio, 1999).
27. Y. Sofue and V. Rubin, *Ann. Rev. Astron. Astrophys.* 39, 137 (2001).
28. O. Wucknitz, A. D. Biggs, and I. W. A. Browne, *Mon. Not. R. Astron. Soc.* 349, 14 (2004).
29. T. York, N. Jackson, I. W. A. Browne, et al., *Mon. Not. R. Astron. Soc.* 357, 124 (2005).